

Boudreau, Mathieu PhD Thesis

Chapter 2

Background

1.1 Multiple Sclerosis

1.1.1 Overview

Multiple sclerosis (MS) is an autoimmune disease that attacks the central nervous system. Canada has one of the highest prevalence of MS in the world [1], where approximately 1 in 340 Canadians have MS [2]. Affecting women disproportionately relative to men (3:1), the rate of incidence has also been observed to increase in the last century [3]. The origin of the disease remains unknown, however both environmental and genetic factors have been shown to increase the risk of getting the disease [4-6]. Populations of countries at higher latitudes have a higher incidence rate of MS [7-9], and individuals are at a higher risk if an immediate family member also suffers from the disease (up to a 25% for identical twins) [10]. Clinical onset of MS mostly begins between the ages of 15 and 40 [11]. Typical physical and cognitive symptoms include vision problems, incoordination, fatigue, difficulty speaking and/or swallowing, pain, spasms, depression, and impaired information processing speeds [12,13]. For most people living with MS, symptoms will initially be temporary (called “attacks” or “flare-ups”) lasting between days up to several months [14], with partial or complete recovery of the disabling symptoms; this stage of MS is called relapse-remitting multiple sclerosis (RRMS). This is followed by the secondary progressive multiple sclerosis (SPMS) stage later on in life, when there is a gradual increase in disability over time, even between attacks. There is no cure for MS. Treatment strategies

mostly involve drug therapies to reduce the frequency of attacks (e.g. interferon beta-1a) or hasten recovery after an attack has already begun (e.g. corticosteroids) [15]. One particularly promising recent Canadian study reported that stem-cell treatment after immunoablation was effective at suppressing long term inflammatory activity in a population with early-aggressive MS [16]. Development of drug therapies that promote remyelination is also an active area of research [17,18], and one of the important challenges in this field is accurately quantifying the myelin regeneration *in vivo*. Clinical MRI techniques typically used for diagnosing MS are not specific enough to myelin density for this purpose; quantitative MRI techniques are expected to emerge as a useful tool for remyelination quantification in clinical trials [18,19].

The mechanisms regulating damage in MS are still not completely understood. Broadly, demyelination in MS white matter (WM) lesions is believed to be a result of an immunologically-mediated attack on myelin and oligodendrocytes [20,21]. In active MS lesions, T-cells mistakenly recognize myelin antigens as a foreign body and respond by emitting cytokines, attracting more lymphocytes to the site which disrupts the blood-brain barrier and amplifies the immune system response. Macrophages responding to the released cytokines in turn destroy the myelin sheaths. Following this immunological response, if some local oligodendrocytes are still present, some remyelination may occur [22]. However, after repeated attacks, irreversible damage such as axonal degeneration and axon transection will occur. Several other pathological characteristics have been observed over the course of the disease progression, such as gliosis (scarring), degeneration of the distal segment of transected axons (Wallerian Degeneration), abnormalities in the non-lesion WM (normal appearing white matter - NAWM), brain atrophy, and cortical lesions.

Although MS has mostly been described as a WM disease, post-mortem histological studies have reported that cortical grey matter (GM) is also abnormal in MS patients. GM lesions are characterized by demyelination, axonal and dendritic transection, neuronal apoptosis and limited inflammatory cell content compared to WM lesions [23,24].

1.1.2 Role of MRI in MS

Since 2001, the gold standard criteria for diagnosing MS with MRI has been the McDonald Criteria [25], subsequently getting two revisions in 2005 and 2010 [26,27], with a most recent update in 2016 by the European group MAGNIMS (Magnetic Resonance Imaging in MS) [28]. These criteria require that hyperintense lesions in T₂-weighted MRI images be observed to disseminate in space (three out of the following lesions: at least 3 periventricular, 1 cortical/juxtacortical, 1 infratentorial, 1 optic nerve, or 1 spinal cord) and in time (new lesions relative to a previous scan). In addition, these can both be determined in a single imaging session if a gadolinium-enhancing T₁ lesion is observed, instead of the dissemination in time condition mentioned above (suggesting a disruption in the blood-brain barrier of an early lesion). It's important to note that the presence of a lesion in one part of the brain is not always a predictor of a symptom in the corresponding anatomical/physiological region [29], and that the criteria above is not sufficient in itself for diagnosing MS. MRI provides an additional tool for the diagnostics of MS when supplementing the patient's history and a physical exam performed by a neurologist [30].

Beyond clinical MRI, there are numerous other MRI techniques that are widely used to study MS in research settings, of which we will mention a select few here. Brain atrophy in MS has been shown to correlate more with disability than clinically identified lesions

[31,32], and can be estimated with manual or automated tissue segmentation using structural images (e.g. T₂-weighted fluid attenuated inversion recovery – FLAIR) [33,34]. Magnetization transfer and diffusion tensor imaging have both demonstrated better sensitivity to abnormalities in NAWM [35,36], which is widespread throughout the brain and in regions preceding lesion formation. In post-mortem studies, diffusion and magnetization transfer metrics have both been shown to correlate with myelin content and axonal count [37-39]. Blood-oxygen-level dependent (BOLD) functional MRI (fMRI) has been used in MS to study cognitive dysfunctions and motor/cognitive reorganization during the disease progression [40,41]. Lastly, the role of GM pathology in MS has been increasingly investigated for its possible role in cognitive dysfunction which become evident during the progressive stage of the disease. Although cortical GM has low myelin content relative to WM, magnetization transfer techniques have demonstrated sensitivity to demyelination in cortical GM lesions [42,43] and as a useful tool to investigate and/or segment cortical lesions and atrophy [44-46].

1.2 Quantitative MR Imaging

Prior to presenting the theory behind quantitative MT (qMT) imaging, which is the focus of this thesis, several other quantitative imaging techniques must be discussed, as qMT requires these measurements for calibration and to constrain fitting parameters. The following section briefly presents the relevant tissue and field properties of interest for qMT, and explains the measurement techniques for these that are relevant for the manuscripts in the later chapters. Countless other quantitative measurement techniques for these properties exist, but are not presented here.

1.2.1 Tissue Properties (T_1 , T_2)

Longitudinal Relaxation Time (T_1)

The longitudinal (or spin-lattice) relaxation time (T_1) is a value that describes how rapidly longitudinal magnetization (M_z) returns to its thermal equilibrium values (M_0) after excitation. The relaxation rate ($R_1 = 1/T_1$) is sometimes defined instead of T_1 . For the simplest case (e.g. liquids), this behavior is mono-exponential, whereas longitudinal relaxation in solids typically behave non-exponentially [47]. At clinical field strengths, T_1 is approximately several seconds for liquids, near one second for soft tissues, and between one and several seconds for solids. T_1 has a dependency on field strength (proportionally) for the range commonly to image humans (1 to 9 Tesla), because nearby spins must create higher frequency fluctuating magnetic fields to exchange energy (relaxation) because of to the higher energy level differences of the spins (Zeeman effect) at high field strength. For example, one study measured T_1 values at 1.5/3.0/7.0 Tesla to be 650/840/1,130 ms for WM and 1200/1600/1940 ms for GM. Knowledge of T_1 values for tissues is important in several applications, such as optimizing pulse sequences for signal-to-noise (e.g. in steady-state pulse sequences), for maximum contrast (e.g. FLAIR), and to assist the estimation of other quantitative parameters (e.g. dynamic contrast enhancement – DCE [48,49]). For qMT, T_1 is a necessary parameter to constrain several fitting parameters in the model which will be discussed later.

The most widely known T_1 mapping pulse sequence, generally considered the gold standard, is Inversion Recovery (IR) [50,51]. A simplified pulse sequence diagram for IR is presented in Figure 0-1. In this experiment, the longitudinal magnetization is initially inverted with an inversion pulse (180°). After a certain time interval (inversion time – TI)

to allow the longitudinal magnetization to relax towards its equilibrium state, an excitation pulse (typically 90°) is applied and k-space data is acquired. By repeating this experiment for several TI values (allowing for a wide range of different longitudinal relaxation amounts to occur), an estimate of T_1 can be determined by fitting the image data voxel-wise for each TI. The IR data can be fitted using a number of different equations, and an overview of them are covered in depth by Barral et al. [52]. For complex data (magnitude & phase), the fitting equation that was demonstrated to be most robust against inaccuracies of the inversion and saturation flip angles and to shorter TRs (shorter than the $TR \approx 5T_1$ needed for full recovery [52,53]) is the following 5-parameter model, which assuming a single tissue/ T_1 within the voxel:

$$I_n = a + be^{-\frac{TI_n}{T_1}} \quad (2-1)$$

where a and b are complex fitting parameters and I_n is the complex voxel-wise signal value for the n^{th} TI measurement (TI_n). If only magnitude data is available, a modified version of Eq. (2-1) must be used, which is too cumbersome to be explained here (see Eqs. 20-24 of Ref. [52]). Note that IR fitted using this form, unlike some other forms of Eq. 2-1, is very robust against flip angle-inaccuracies/ B_1 -inaccuracies [52,53]. Inversion recovery is typically limited to a single-slice technique in practice, because it requires a long TR value ($TR > T_1$) relative to other steady-state techniques. Modified inversion recovery T_1 mapping techniques have been developed to accelerate the acquisition, such as Look-Locker [54,55], which acquires several TIs within a single TR using a small flip angle. Another inversion recovery-based T_1 mapping technique that has become increasingly used due to its availability as a standard MRI scanner pulse sequence over the course of this

this work is Magnetization Prepared 2 Acquisition Gradient Echo (MP2RAGE) [56]. MP2RAGE simultaneously acquires a T_1 -weighted map and a T_1 map, is a B_1 -independent measurements like IR, and has potential applications for MS research [57].

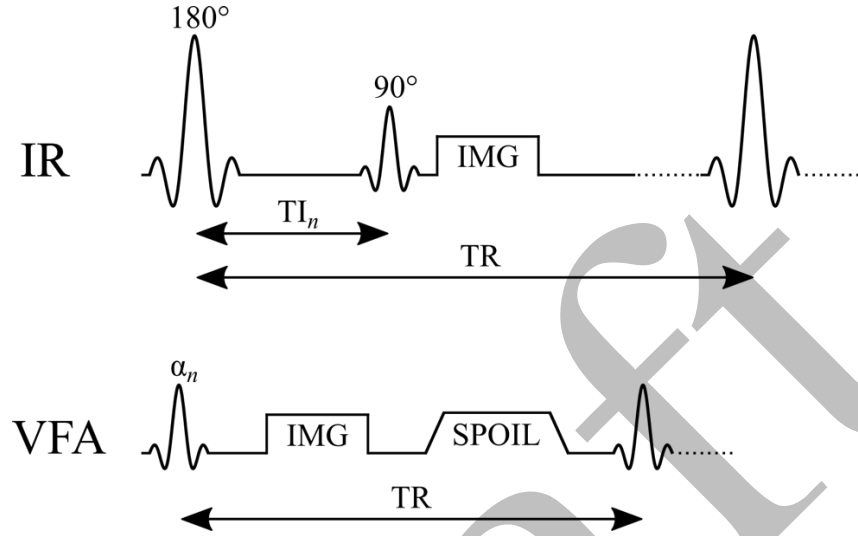


Figure 0-1. Simplified pulse sequence diagrams of two T_1 mapping techniques: Inversion Recovery (IR) and Variable Flip Angle (VFA). TR: repetition time, TI: inversion time, α : excitation flip angle, IMG: image acquisition (k-space readout), SPOIL: spoiler gradient.

Variable Flip Angle (VFA) is alternative T_1 mapping technique that is capable of mapping T_1 throughout the brain in a clinically feasible acquisition time by using a steady-state imaging spoiled gradient echo (SPGR) approach [58,59]. VFA is sometimes also called DESPOT1 (Driven Equilibrium Single Pulse Observation of T_1) [60]. A simplified pulse sequence diagram for VFA is presented in Figure 0-1. This technique takes advantage of the fact that the SPGR acquisition signal for short TR ($TR \ll T_1$, in the tens of ms range) is very sensitive to the excitation flip angle (α) and T_1 . By acquiring SPGR images using different flip angles, the T_1 values within a voxel can be estimated by fitting the magnitude image data to the steady-state SPGR signal equation:

$$I_n = K \frac{1 - e^{-\frac{TR}{T_1}}}{1 - \cos \alpha_n e^{-\frac{TR}{T_1}}} \sin \alpha_n \quad (2-2)$$

where K is a constant that contains tissue density and receiver coil sensitivity information. Although T_1 could be estimated by fitting Eq. (2-2) using non-linear curve fitting algorithms, which can be time-consuming for high-resolution whole-brain scans, the terms in this equation can be rearranged so that a solution can be found in terms of a linear equation of the form $y = mx + b$ [53]:

$$\left(\frac{I_n}{\sin \alpha_n} \right) = e^{-\frac{TR}{T_1}} \left(\frac{I_n}{\tan \alpha_n} \right) + \text{constant} \quad (2-3)$$

where the constant does contain T_1/TR values, but not α_n or I_n [58]. Because α_n and TR are both known values, this equation can be solved for T_1 rapidly by linear fitting for a minimum of two flip angles (slope = $e^{-\frac{TR}{T_1}}$). However, one caveat of this method is that, due to its sensitivity to the flip angle, it is a B_1 -dependent T_1 mapping method; a B_1 map must be acquired to scale the nominal flip angles to its correct value to accurately estimate T_1 using VFA. One advantage of VFA T_1 mapping is that SPGR is a standard pulse sequence on most MRI scanners, making whole-brain T_1 mapping accessible to a wide range of researchers and clinicians contingent on if they also acquire a B_1 map, which is not always the case [61], particular for DCE studies [49,62,63].

Transversal Relaxation Time (T_2)

The transverse (or spin-spin) relaxation time (T_2) is a value that describes how rapidly transverse magnetization (M_{xy}) returns to its thermal equilibrium values (zero) in the

absence of static magnetic field inhomogeneities. For the simplest case (e.g. liquids), this behavior is mono-exponential. T_2 is typically smaller or equal to T_1 , exceeding this limit only under very extreme circumstances [64-67]. In general, T_2 is longer in liquids (~seconds) than in solids (~microseconds), and tissues have an intermediate T_2 range of 25-100 ms [68]. Macromolecules, such as proteins and lipids in myelin, have T_2 values closer to solids (~10 microseconds) [69], due to a longer rotational correlation time of hydrogen in these molecules [70]. T_2 does not have a strong dependence on field strength (unlike T_1); however, T_2^* – the apparent T_2 in the presence of static field inhomogeneities – does have a strong inversely proportional relationship with main magnetic field strength in humans [71].

qMT does not require a quantitative T_2 map for calibration or to be a constraint. However, most qMT models do inherently fit the data for T_2 values. In the two-pool qMT model (to be discussed in detail later), qMT models typically have two different T_2 fitting parameters: T_2 of the “free-pool” ($T_{2,f}$, on the order of milliseconds) and T_2 of the “restricted pool” ($T_{2,r}$, on the order of microseconds). Some groups choose to fix the $T_{2,r}$ values to the average whole-brain value in their fitting models [72], in part because histopathology studies have not observed a correlation between $T_{2,r}$ and myelin density [39]. Nevertheless, quantitative T_2 mapping is an important technique for MS, as it is used to estimate the myelin water fraction (MWF) [73,74], a measure that has been shown to correlate with myelin content [75,76]. MWF is calculated as the ratio of T_2 distribution of water trapped between the myelin layers (~40-50 ms) over the T_2 distribution of intra/extracellular water (~100 ms). These T_2 distributions are typically estimated by fitting multi-component T_2

signal decay curves with multi-echo spin-echo pulse sequences; a comprehensive technical review of MWF acquisition methods is presented in Alonso-Ortiz et al. 2015 [77].

1.2.2 Field Properties (B_0 , B_1)

B_1 Mapping

The transmit radio-frequency (RF) amplitude (“ B_1^+ ”, but more frequently written simply as “ B_1 ” in the context of quantitative MRI imaging) is a quantity that directly impacts the actual flip angle that magnetization in a voxel rotates due to an on-resonance RF pulses. Spatial inhomogeneity of B_1 leads to spins across the sample experiencing different flip angles, which can lead to differences in image signal intensity throughout a homogeneous sample. Although B_1 can refer to the actual RF magnetic field amplitude (on the order of microteslas [78]), in the context of quantitative MRI it’s more represented as a normalized correction factor of the nominal flip angle set by the user at the scanner ($\alpha = B_1 \cdot \alpha_{\text{nominal}}$). B_1 maps are measured as a calibration measurement for quantitative MRI techniques, however some interesting parameters can be derived directly from B_1 maps, such as the electrical conductivity and permittivity of tissues [79] and the local spectral absorption rate (SAR) [80]. Even if B_1 is calibrated to a high degree of homogeneity in an empty scanner (e.g. using pickup coils and coil design optimization), electrodynamic interactions with tissues (loading/boundaries) will distort the B_1 amplitude profile [81]. For a human head, this pattern is generally elliptical [82]. B_1 -inhomogeneity is also heavily influenced by field strength due to the lengthening of the RF wavelength, worsening at higher field strengths. B_1 inhomogeneity is particularly a challenge at ultra-high fields (7T+) due to an RF wavelength on the order of the size of the human head, leading to constructive/destructive interference of the RF wave [83].

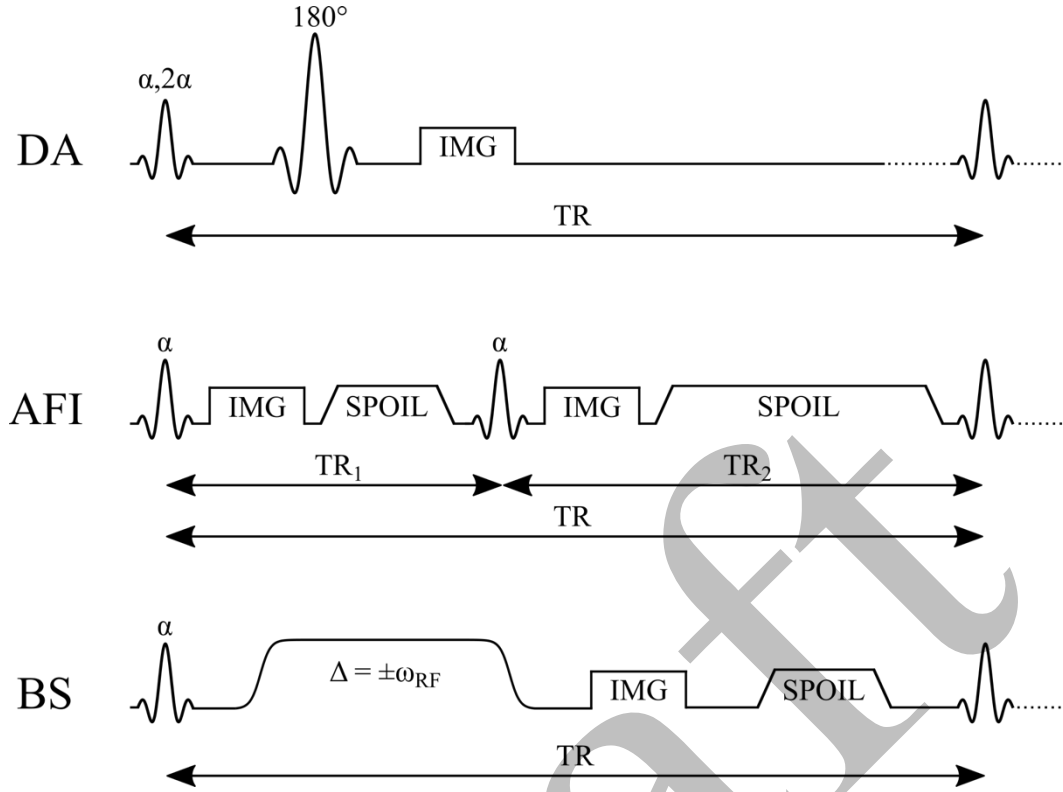


Figure 0-2. Simplified pulse sequence diagrams for three widely used B_1 mapping methods: Double Angle (DA), Actual Flip angle Imaging (AFI), and Bloch-Siebert shift (BS). TR: repetition time, α : excitation flip angle, Δ : off-resonance frequency, IMG: image acquisition (k-space readout), SPOIL: spoiler gradient.

One of the simplest ways to map B_1 in vivo is to acquire two images using different excitation flip angles. The actual voxel-wise flip angles can be then estimated with simple trigonometry, by calculating the ratio in expected signal amplitudes. Using the Double Angle (DA) method, one image is acquired with double the excitation flip angle than the other, which results in a very simple equation for a spin-echo acquisition pulse sequence (Figure 0-2) [84,85]:

$$B_1^{DA} = \frac{\arccos\left(\frac{I_{2\alpha}}{2I_\alpha}\right)}{\alpha} \quad (2-4)$$

Another implementation of the DA method uses a spin-echo pulse sequence with an inversion pulse of 2α instead 180° , since some MRI scanner manufacturer set their spin-

echo pulse sequence to be $\alpha-2\alpha$. The equation for the DA B_1 differs from the one above, and is presented in Wang et al 2005 [86]. DA B_1 mapping is easy to implement using pulse sequences available on most scanner. However, to minimize the influence of T_1 relaxation in the region of interest, it requires a long TR (at least longer than a few T_1 's [85], but ideally $TR \geq 5T_1$), usually limiting the pulse sequence to a single-slice technique. Other pulse sequence variations of the double angle technique have also been developed, to improve acquisition properties like acquisition time [86,87] and slice profile effects [88].

Numerous rapid whole-brain B_1 mapping techniques have been developed over the years. Two popular and highly cited techniques to have emerged in the past decade is Actual Flip angle Imaging (AFI) [89] and Bloch-Siegert (BS) shift [90] B_1 mapping (Figure 0-2). AFI is a 3D technique implemented using a steady-state imaging approach, whereas BS is a phase-based imaging technique. The AFI pulse sequence is a SPGR-based technique, in which within a single TR, two acquisitions occur with different delays before the following excitation pulse (TR_1 and TR_2 , $TR_1 \neq TR_2$). The steady-state signal for each acquisition will be different because of the different durations allowed for relaxations relative to the previous excitation pulse. If TR_1 and TR_2 are both very short relative to T_1 , B_1 can be calculated from the following equation [89]:

$$B_1^{AFI} = \frac{\arccos\left(\frac{rn-1}{n-r}\right)}{\alpha} \quad (2-5)$$

where $r = \frac{I_2}{I_1}$ and $n = \frac{TR_2}{TR_1}$. B_1 calculated from AFI is very insensitive to T_1 values [89], however it can be sensitive to incomplete RF and gradient spoiling [91,92]. The AFI pulse sequence is currently not typically available by default on most MRI scanners, and must

be implemented on-site by an MRI pulse sequence programming expert. Despite some drawbacks, it is used in a wide array of applications, particularly for B_1 mapping at very high fields strengths [93-96].

BS is a phase-based B_1 mapping technique that uses the Bloch-Siegert shift phenomenon. The Bloch-Siegert shift is a change in experienced precession frequency of spins in the presence of an off-resonance RF field, sufficiently off-resonance so that no longitudinal \leftrightarrow transversal rotation occurs. Conceptually, the spins in the rotating frame at the off-resonance frequency of the RF pulse experience a non-zero B_z vector field, and far off-resonance this vector component will dominate over the B_1 field in transverse plane, such that the spins will precess about B_z at a rate proportional to the B_1 amplitude. This effect also results in a phase accrue ment, which is also dependent to the B_1 amplitude of the off-resonance RF pulse. Typically, BS B_1 mapping is implemented by acquiring two images each using symmetrically off-resonance RF pulses ($\Delta=\pm\omega_{RF}$), applied between the excitation pulse and readout (Figure 0-2). B_1 values can be calculated from this experiment using the following equations [90]:

$$B_1^{BS} = \frac{\sqrt{\frac{\phi_+ - \phi_-}{2K_{BS}}} \int_0^T \gamma B_{1,normalized}(t) dt}{\alpha} \quad (2-6)$$

$$K_{BS} = \int_0^T \frac{(\gamma B_{1,normalized}(t))^2}{2\omega_{RF}} dt \quad (2-7)$$

where ϕ_+ is the voxel phase value for the $\Delta=+\omega_{RF}$ acquisition, ϕ_- is the voxel phase value for the $\Delta=-\omega_{RF}$ acquisition, and γ is the gyromagnetic ratio of the spin population, T is the

total duration of the off-resonance pulse, α is the excitation pulse flip angle, and $B_{1,normalized}$ is the pulse profile of the off-resonance B_1 pulse ($B_{1,normalized} = B_1/B_{1,max}$). The off-resonance RF pulse is typically very long (~5-10 ms) relative to the excitation pulse, and has a wide Fermi or Gaussian profile so that the spins experience a very small frequency band in practice (as a consequence of Fourier theory). BS also exhibits very low sensitivity to T_1 effects [90]; however, it is dependent on reliable phase unwrapping, which can be challenging in the presence of phase artifacts like fringe lines and phase poles [97]. Conventional BS imaging has very high SAR, which is a potentially limiting factor for high field applications, although some modifications to the technique have been proposed to make BS feasible at high field strengths [93,98].

B₀ Mapping

The local main magnetic field (B_0) influences the resonant precession frequency of spins. In principle, it is much simpler to quantify B_0 compared to other quantitative MRI parameters. Most scanners come equipped with at least one pulse sequence to acquire B_0 or a field map; this information is used during the shimming process of MRI scanners. The simplest pulse sequence used for acquiring B_0 is a basic SPGR pulse sequence by acquiring two images at different echo times (TE). Using a phase subtraction technique, B_0 – which in quantitative MRI is usually in terms of a frequency – can be calculated from the following equation [99]:

$$B_0 \equiv \Delta\omega_0 = \frac{\Delta\phi}{\Delta TE} \quad (2-8)$$

where φ is the phase in radians. For high B_0 or ΔTE values, the phase can exceed $\pm\pi$ radians, and the phase images will require phase unwrapping prior to calculating the difference, which can be challenging if certain artifacts are present (e.g. fringe lines & poles). Also, the B_0 field inhomogeneity can be caused by pulse sequence-specific factors, for example Eddy currents induced in the MRI hardware as a result of strong time-varying magnetic field gradients. Thus, for B_0 correction in quantitative MRI, it may be desirable to use a B_0 mapping pulse sequence that more closely reproduces the magnetic field environment of the quantitative MRI pulse sequence being used.

1.3 Magnetization Transfer Imaging

1.3.1 Two-Pool Model of MT

The largest contribution of signal from conventional MRI experiments originate from hydrogen in water molecules, which is plentiful and dense in most human organs and generally has a slow signal decay (~ 10 to 100 ms), allowing sufficient time for an imaging experiment. Hydrogen is also present in numerous other molecules, such as macromolecules (lipids and proteins) in myelin. However, MRI signal from hydrogen in these macromolecules decay very quickly ($T_2 \sim \mu s$) due to their semi-solid nature and long rotational correlation times, making it very challenging to directly image myelin content. Another consequence of the short T_2 for these macromolecules is a very broad spectrum of resonant frequencies (~ 10 's of kHz). In the 1970s and 1980s, researchers discovered that by selectively exciting the macromolecular hydrogen with off-resonance RF pulses prior to an NMR/MRI acquisition, longitudinal magnetization from water hydrogen is transferred to nearby macromolecules through a process called cross-relaxation, resulting

in a lower MRI signal in regions where there is an abundant quantity of macromolecules near water [100-102]. This discovery lead to the development of the two-pool model of magnetization transfer model (Figure 0-3), where magnetization from hydrogen in water is referred to as the “free-pool”, and macromolecular hydrogen is referred to as the “restricted-pool”.

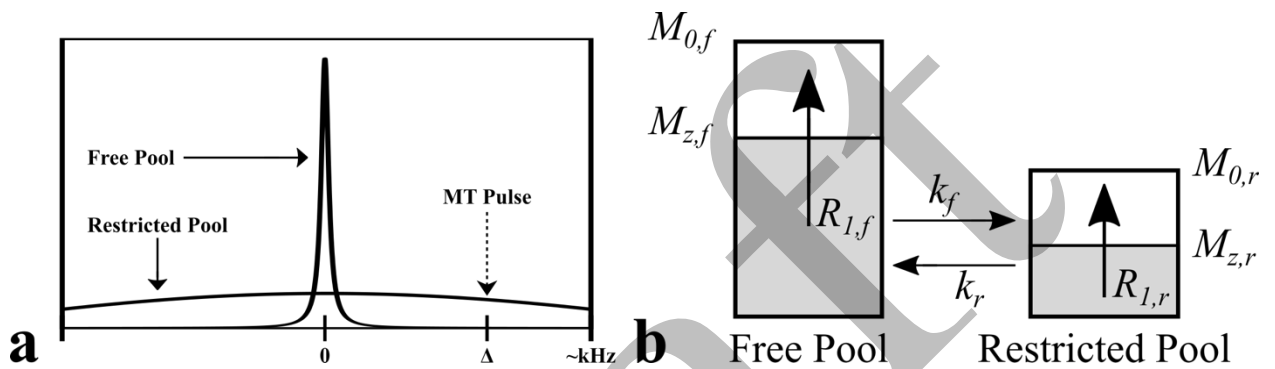


Figure 0-3. Two-pool model of the magnetization transfer effect. a – example relative spectral lineshapes for “free pool” hydrogen (e.g. in water) and “restricted pool” hydrogen (e.g. macromolecules in myelin). b – evolution of the magnetization of the two pools during the exchange process. $M_{0,f}$: equilibrium magnetization of the free pool, $M_{z,f}$: longitudinal magnetization of the free pool, $M_{0,r}$: equilibrium magnetization of the restricted, $M_{z,r}$: longitudinal magnetization of the restricted pool, k_f : magnetization transfer exchange rate from the free pool to the restricted pool, k_r : magnetization transfer exchange rate from the restricted pool to the free pool, $R_{1,f}$: longitudinal relaxation rate of the free pool, $R_{1,r}$: longitudinal relaxation rate of the restricted pool.

Conceptually, the magnetization transfer effect as discussed above and presented in Figure 0-3 is somewhat puzzling, since unlike energy and momentum, the net magnetization is not a conserved quantity. For example, if a 90° excitation pulse is applied followed by a strong crusher gradient, the equilibrium magnetization vector $M_0\hat{z}$ is converted to the null vector $\hat{0}$. In reality, it is more specifically *energy* of the spin populations between the two pools that is exchanged during the MT phenomenon, and the longitudinal magnetization of each pool differ as a result this energy exchange, leading to an observed magnetization transfer. Figure 0-4 displays the energy level diagrams of two spin populations at three

different stages of a magnetization transfer experiment. For simplicity, the relaxation rates of each pool are neglected in this diagram (which in reality are present).

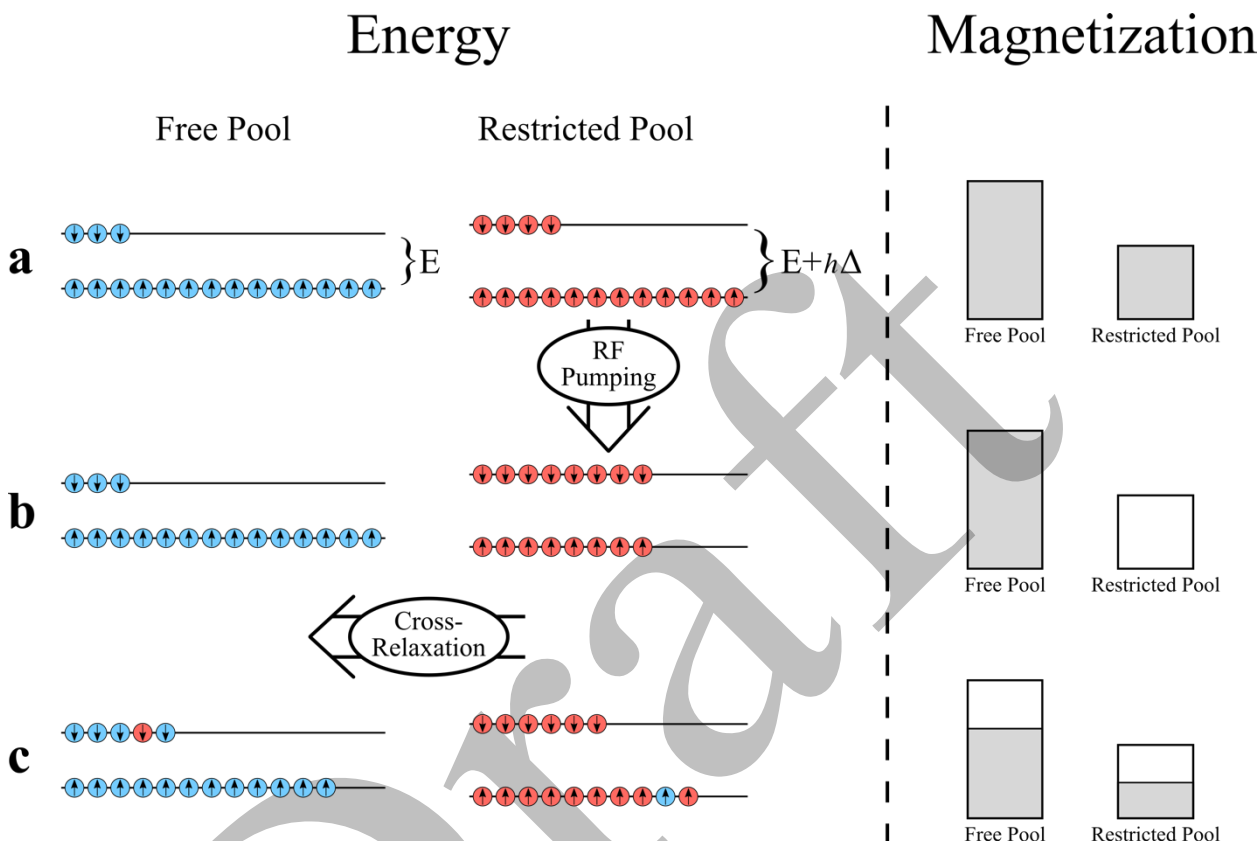


Figure 0-4. Energy level (left) and magnetization (right) diagrams of restricted and free pool hydrogen a) at thermal equilibrium, b) after an off-resonance pulse that pumps energy into the restricted pool, and c) after cross-relaxation/MT-exchange, which distributes excess spin energy from the restricted pool amongst both spin populations through dipole coupling (spin remain in the same pool) or chemical exchange (spin switch pools).

Considering an initial condition of thermal equilibrium, the spin populations for both pools are distributed unevenly between the two energy levels caused by Zeeman splitting for spins in an external magnetic field (Figure 0-4a – left). An excess of spins in the low energy levels result in non-zero total longitudinal magnetization vectors (M_z) of $M_{0,f}$ and $M_{0,r}$ for the free and restricted pools (Figure 0-4a – right). The restricted pool can be selectively saturated by using an off-resonance pulse, without impacting the energy of the free pool

(Figure 0-4b; however, in practice there is some saturation of the free pool that needs to be modeled). The excess energy pumped into the restricted pool in this example reduces the total longitudinal magnetization vector of the spins to zero. Lastly, over time the excess energy pumped into the restricted pool will dissipate to nearby hydrogen spins in the free pool by a stochastic process, through phenomena such as dipolar-coupling and chemical exchange. The excess energy lost by the restricted pool results in an increase in longitudinal magnetization, while the excess energy gained by the free pool results in a reduction in longitudinal magnetization, resulting into an apparent magnetization exchange from the free pool to the restricted pool. The two-pool model is a simplified version of the phenomenon; a four-pool model (myelin water, intra/extra cellular water, myelin semi-solids, non-myelin semi-solids) has also been proposed, as it modeled in MWF imaging. However, it's been shown that the two-pool model is sufficient to model quantitative MT phenomenon in WM [103]. Lastly, although the description above was framed in terms of an MT experiment, any pulse sequence that exposes macromolecules to off-resonance RF fields can result in an MT effect, such as standard multislice imaging [104,105].

1.3.2 *MTR and MTsat*

Magnetization Transfer Ratio (MTR)

The simplest and most widely used measure of the magnetization effect is the magnetization transfer ratio (MTR). In this experiment, two images are acquired with (I_{MT}) and without (I_0) an off-resonance RF pulse preceding the imaging pulse sequence, and MTR is the normalized difference of these two images calculated in terms of a percentage:

$$\text{MTR} = \frac{I_0 - I_{MT}}{I_0} \cdot 100 \quad (2-9)$$

As discussed in the previous section, the greater the MT effect (e.g. more macromolecular content), the less I_{MT} values will be, resulting in higher MTR values. In the context of MS, demyelinated lesions are expected to have lower MTR voxel values relative to normal appearing white matter (NAWM). An example MT imaging pulse sequence (MT-prepared SPGR) is shown in Figure 0-5. In this pulse sequence, a conventional short-TR SPGR pulse sequence is preceded by a long off-resonance RF pulse with a widely shaped pulse envelope. Prior to the excitation RF pulse (on-resonance) of the SPGR imaging sequence, a spoiler gradient is applied to eliminate any potential free-pool (long T_2) magnetization that was excited by the MT pulse and rotated into the transverse plane as well as any residual transverse magnetization from the excitation pulse of the previous TR. For the MT-off image (I_0), the same pulse sequence timing and gradients are used, but without the off-resonance RF pulse.

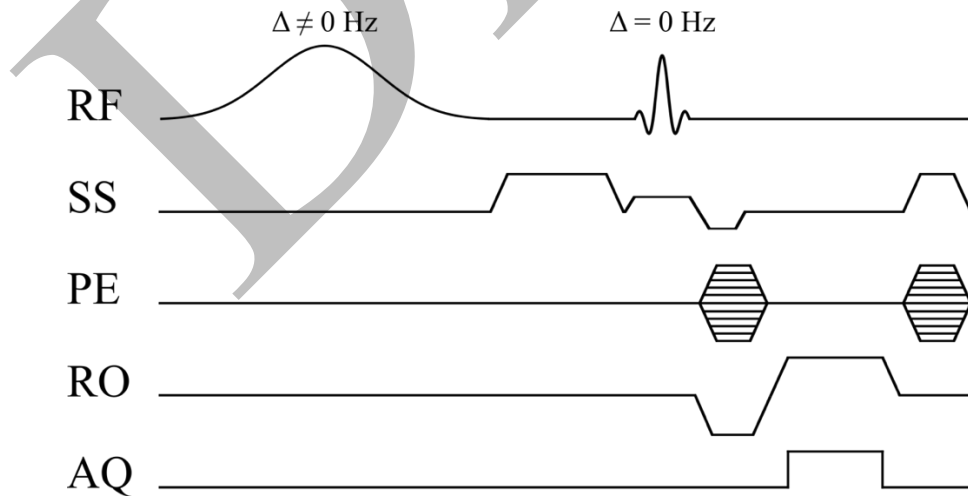


Figure 0-5. Pulse sequence diagram for a pulsed MT-weighted spoiled gradient echo (SPGR) pulse sequence with a Gaussian MT pulse shape. RF: radiofrequency pulse, SS: slice-selecting gradient, PE: phase-encoding gradient, RO: readout gradient, AQ: data acquisition.

MTR pulse sequences are available on most clinical MRI scanners, making it an accessible imaging tool for researcher and clinicians. Due to its simplicity in implementation and computation, it is possible to produce a whole-brain high-resolution MTR maps in a clinically feasible time. However, MRI manufacturers often impose a fixed off-resonance frequency, effective MT pulse flip angle, and MT pulse shape envelope to their MT pulse sequences, all of which influence the MT effect and resulting MTR values. Because the values for these parameters are not standardized between MRI manufacturers, the MTR values for tissues/lesions can differ substantially between imaging sites. One large multi-center study previously observed MTR values at 1.5T in WM ranging between 9% and 51% [106], and as a result standardized protocols have been proposed [107,108]. MTR is not solely sensitive to macromolecular density; it groups all the factors that impact the MT-prepared SPGR steady-state signal into a single value, such that MTR is also sensitive to effects such as B_1 inhomogeneity and local T_1 values. Thus, MTR is typically referred to as a semi-quantitative MRI measure. Researchers have proposed corrective factors for MTR maps, in particular for B_1 inhomogeneity [87,109]. However, requiring a B_1 map increases the acquisition time, and B_1 mapping pulse sequences are not always available on clinical scanners as a default setting, reducing the accessibility of B_1 -corrected MTR for researchers and clinicians. The impact of T_1 on MTR is also an important consideration, as it varies not only between tissues but also due to other biological processes, such as inflammation and edema that can occur in MS lesions [110]. Disassociating these effects with demyelination can be challenging (or impossible) for an MTR measurement. Despite some drawbacks, MTR has been shown to correlate significantly with myelin density and axonal count in post-mortem MS brains using immunohistopathology [38,111], and has

been widely used for in vivo MS research studies to infer on de/re-myelination monitoring [19,112-114], diffuse NAWM/NAGM and GM pathology [45,115-121], and therapeutic clinical trials [122-125]. Beyond MS applications, several other diseases with neurological manifestations have been studied using MTR, such as schizophrenia [126,127], HIV [128], Alzheimer's disease [129], and major depressive disorder [130].

Magnetization Transfer Saturation (MTsat)

Another semi-quantitative measure of the MT effect is the magnetization transfer saturation (MTsat) value [131]. MTsat is an emerging MT technique with inherent compensation for B_1 profile effects and lower sensitivity to T_1 differences, and has the same potential applications for MS research as were listed above for MTR. Unlike MTR, which is the normalized difference of the steady-state signal with and without an MT-preparation RF pulse, MTsat is an estimate of the fractional longitudinal magnetization reduction caused by the MT pulse within a single TR (after a steady-state has been established). MTsat only requires one additional measurement to the two SPGR-MTR acquisitions; one T_1 -weighted SPGR scan with different TR/ α values (\downarrow/\uparrow , respectively) with no MT pulse. From these three measurements (S_{PD} : MT-off SPGR, S_{MT} : MT-on SPGR, S_{T_1} : T_1 -weighted SPGR), MTsat can be calculated directly with the following equations [131,132]:

$$MTsat = \left(A_{app} \cdot \frac{\alpha_{MT}}{I_{MT}} - 1 \right) R_{1,app} TR_{MT} - \frac{\alpha_{MT}^2}{2} \quad (2-10)$$

$$A_{app} = I_{PD} I_{T_1} \frac{TR_{PD} \frac{\alpha_{T_1}}{\alpha_{PD}} - TR_{T_1} \frac{\alpha_{PD}}{\alpha_{T_1}}}{TR_{PD} I_{T_1} \alpha_{T_1} - TR_{T_1} I_{PD} \alpha_{PD}} \quad (2-11)$$

$$R_{1,app} = \frac{1}{2} \cdot \frac{\frac{I_{T_1} \alpha_{T_1}}{TR_{T_1}} - \frac{I_{PD} \alpha_{PD}}{TR_{PD}}}{\frac{I_{PD}}{\alpha_{PD}} - \frac{I_{T_1}}{\alpha_{T_1}}} \quad (2-12)$$

where α is the excitation flip angles in radians, and TR is the repetition times in seconds. MTsat calculated in Eq. (2-10) is a fractional value ($\sim 10^{-2}$), which is sometimes expressed in percentage units (as is done with MTR) by multiplying by 100. Because both MTR and MTsat can both be expressed as percentage units, there is a risk of confusion when interpreting MTsat values relative MTR. MTsat is substantially lower than MTR in tissues (by a factor of ~ 10), because it represents the fractional signal saturation from a single MT pulse and not the overall steady-state signal differences like MTR. Another caveat of MTsat is that its interpretation is linked to the effective flip angle of the MT pulse, making it challenging to interpret MTsat values reliably between sites if they use different acquisition protocols. Nonetheless, MTsat is very simple to implement, only requires one additional measurement relative to MTR, and could be an accessible alternative to MTR for researchers in need of a semi-quantitative MT measure with more robustness against B_1 and T_1 . MTsat has been shown to correlate better with MS disability levels than MTR in NAWM and the spinal cord [133], and has a more linear correlation with the pool-size ratio (restricted/free) than MTR [134]. It has also been used for other applications, such as g-ratio measurement (ratio of the inner/outer diameter of the myelin sheath of an axon) [134,135], segmentation of deep grey matter structures [136], and hypomyelinating disorders [137].

1.3.3 Quantitative Magnetization Transfer Imaging

Quantitative measurement of the magnetization transfer effect requires a mathematical model describing the evolution of the magnetization/signal throughout an MT experiment. For a two-pool model of exchange (Figure 0-3 and Figure 0-4), the Bloch differential equations describing the coupled cross-relaxation of the magnetization vectors of the free and restricted pools are [101,138-142]:

$$\frac{dM_{x,f}}{dt} = -\frac{M_{x,f}}{T_{2,f}} + \Delta M_{y,f} - \text{Im}(\omega_1)M_{z,f} \quad (2-13)$$

$$\frac{dM_{y,f}}{dt} = -\frac{M_{y,f}}{T_{2,f}} + \Delta M_{x,f} - \text{Re}(\omega_1)M_{z,f} \quad (2-14)$$

$$\frac{dM_{z,f}}{dt} = \frac{(M_{0,f} - M_{z,f})}{T_{1,f}} - k_f M_{z,f} + k_r M_{z,r} + \text{Im}(\omega_1)M_{x,f} - \text{Re}(\omega_1)M_{y,f} \quad (2-15)$$

$$\frac{dM_{z,r}}{dt} = \frac{(M_{0,r} - M_{z,r})}{T_{1,r}} + k_f M_{z,f} - k_r M_{z,r} + W M_{z,r} \quad (2-16)$$

$$W = \pi \omega_1^2 G(\Delta, T_{2,r}) \quad (2-17)$$

where Δ is frequency of the RF pulse, $\omega_1 = \gamma B_1$ is a complex and time-varying function of the RF pulse amplitude, k_f is the magnetization exchange rate from the free pool to the restricted pool, k_r is the magnetization exchange rate from the restricted pool to the free pool, $M_{0,f/r}$ is the equilibrium longitudinal magnetization of the free/restricted pool, and W is the transition rate of the restricted pool in the presence of an off-resonance RF pulse (see Figure 0-4a to b) and assumes a shaped RF pulse with a narrow bandwidth (a more

general expression for W is presented in Ref. [141]). Note that the transverse components (x/y) of the restricted pool are omitted above, as $T_{2,r}$ is much shorter than the typical experimentation time, and studies have shown these terms can be safely neglected [141,143]. An important quantitative MT parameter that is implicitly included in the equations above is the pool-size ratio, $F = M_{0,r}/M_{0,f}$, where by definition $k_r = k_f/F$. In Eq (2-17), G is the spectral lineshape function of the restricted pool (e.g. Figure 0-3a). Common spectral lineshapes observed in restricted pools are Gaussian for solids and gels (e.g. imaging phantoms) and super-Lorentzian for in vivo tissues [143]. One important point to note is that the measured longitudinal relaxation rate ($R_{1,obs} = 1/T_1$) in the presence of macromolecules differs from the free pool longitudinal relaxation rate $R_{1,obs}$, and the relationship between the two is described by:

$$R_{1,f} = R_{1,obs} - \frac{k_f(R_{1,r} - R_{1,obs})}{(R_{1,r} - R_{1,obs}) + \frac{k_f}{F}} \quad (2-18)$$

Equations (2-13) to (2-16) cannot be solved analytically for most quantitative MT pulse sequence experiments. One exception is the case where Eqs. (2.15) and (2.16) are driven to a steady-state using a continuous-wave (“hard” pulses) MT-preparation RF pulse (1 to 5 seconds) prior to data acquisition [140]. However, this technique does not lend itself well to in vivo quantitative MT imaging experiments due to its long acquisition times and high SAR. Pulsed MT pulse sequences, initially proposed using binomial RF pulses with zero net flip angle on-resonance [144,145] followed by the more commonly used shaped off-resonance pulses [141,142,146] (e.g. Figure 0-5), were demonstrated to be a practical alternative to CW for in vivo quantitative MT imaging. One caveat of using a pulsed

approach to qMT is that solving these equations for a pulsed-MT pulse sequence are numerically very difficult, and require exceedingly large computation times to process the several thousand (single-slice) up to several hundred thousand voxels (whole-brain). Several numerical approximations have been proposed to solve Eqs (2.13) to (2.16) in order to fit qMT data for the unknown model parameters: F , k_f , $R_{1,f}$, $R_{1,r}$, $T_{2,f}$, and $T_{2,r}$. Several approximation methods have been developed model the qMT experiment and fit the data quicker [142,147,148]. Most pulsed off-resonance qMT models share two features: (1) $R_{1,r}$ is fixed to 1 s^{-1} , as these types of qMT experiments are largely insensitive to $R_{1,r}$ [140], and (2) a T_1 map ($1/R_{1,\text{obs}}$) is required to constrain the fitting parameters $R_{1,f}$, F , and k_f using Eq. (2-18) [140,142]. Thus, only four free model fitting parameters remain to be solved in a qMT experiment (F , k_f , $T_{2,f}$, and $T_{2,r}$).

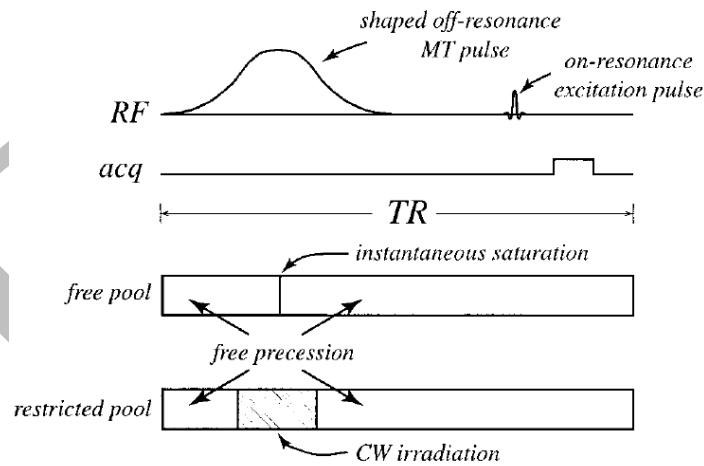


Figure 0-6. Sled and Pike qMT model for a pulsed MT-weighted spoiled gradient echo (SPGR) pulse sequence experiment.

The first qMT fitting model proposed for in vivo imaging of all quantitative fitting parameters was introduced in 2001 for a pulsed-MT SPGR experiment [142], and is often referred to as the Sled and Pike model after its authors. The Sled and Pike model has been shown to produce more accurate estimations of qMT fitting parameters compared to other

qMT models [149], and is the model used throughout this thesis. Figure 0-6 graphically present the approximations used in this model, which are for a pulsed-MT SPGR experiment (Figure 0-5). The effect of both the excitation and the MT pulse on the free pool is approximated as an instantaneous saturation, which is precomputed prior to fitting the imaging data by solving the equations in the absence of relaxation or exchange between pools for a wide range of effective MT flip angles, Δ , and $T_{2,f}$. The second approximations of the Sled and Pike model is in neglecting the effect of the excitation pulse on the restricted pool, and to approximate the shaped MT pulse as a CW pulse of equivalent power and offset frequency. With these assumptions, the evolution of the magnetization can be broken down into event blocks of free precession, CW irradiation at an off-resonance frequency, and instantaneous saturations of the free pool, making it possible to solve the steady-state Bloch equations in a closed-form [141] instead of numerically, substantially improving the fitting time. To fit the qMT parameters in the model, several MT-weighted SPGR image acquisitions are needed at several different off-resonance frequencies (Δ) and effective MT-pulse flip angles (FA_{MT} , the excitation flip angle that would occur if the RF pulse was applied on resonance, and related to ω_1), in addition to one image without an MT pulse (I_0) for data normalization. Plots of normalized MT-weighted data as a function of off-resonance frequencies for each FA_{MT} are typically referred to as a “Z-spectrum”. In addition to the MT data and T_1 map needed to constrain the model parameters, B_0 and B_1 maps are also typically acquired as corrective factors for Δ and ω_1 , respectively. Open-source software to simulate and fit qMT data using the Sled and Pike model (and several other models) was recently published and released online [150].

The qMT parameter that has demonstrated the most potential for inferring information about tissue abnormalities in MS is the pool-size ratio F , which is a measure of the restricted pool size of macromolecular content relative to the local water content. In post-mortem MS brains, F has been shown to significantly correlate with myelin content [39], and significant differences in F were measured between in WM lesions and NAWM, de- and re-myelinated lesions, and between remyelinated lesions and NAWM. This study also suggested that F may be a more specific biomarker for myelin loss than MTR, particularly in NAWM. Several studies have reported significant difference in F in vivo between MS lesions and NAWM/controls [142,147], and in the longitudinal evolution of acute MS lesions [151]. In healthy brains, regional variations of F across different WM/GM regions of the brains have been reported [152], and great scan-rescan reproducibility has been demonstrated [153]. F has also been a good predictor of de/re-myelination in animal models of MS [154,155]. Beyond MS, other potential applications of qMT have been explored, such as Alzheimer's [156], breast imaging [157], cartilage imaging [158], g-ratio imaging [134,159], and the characterization of dry-cured hams [160].

Fitting qMT data for the four quantitative parameters requires several MT and calibration measurements. Initially, 60 MT-weighted images were acquired (with different TRs, FA_{MT} , Δ values) in addition to one normalization measurement with no MT pulse (for each TR). Subsequent studies demonstrated that the four qMT parameters could be fitted reliably using at least 10 MT-weighted measurements, by using protocol-design optimization [161,162]. These MT-weighted SPGR measurements, in addition to the three calibration measurements (B_0 , B_1 , T_1), mostly made qMT limited to a single-slice technique. However, with the development of parallel imaging and compressed sensing rapid acquisition

techniques [163,164], high-resolution whole-brain is rapidly becoming accessible. This means that the calibration measurements (B_0 , B_1 , T_1) used for qMT must also change from single-slice to whole-brain techniques, which may have unintended consequences on qMT parameter estimates. For example, early qMT studies used single-slice T_1 mapping techniques such as Look-Locker (LL) or Inversion Recovery (IR), which are B_1 -independent T_1 mapping methods. For whole-brain qMT imaging, VFA is a more practical choice for T_1 mapping; however, it is a B_1 -dependent technique. Because qMT is also a B_1 -dependent technique, inaccuracies in the B_1 map may impact the qMT fitting estimates differently depending on if a B_1 -independent (e.g. IR) or B_1 -dependent (e.g. VFA) T_1 mapping technique is used. If IR/LL T_1 mapping is used, an error in B_1 will only propagate to qMT through the FA_{MT} and excitation flip angles of the model. Using VFA T_1 , an error in B_1 propagate through this same pathway, but also through the F/k_f parameter constraint in Eq. (2-18) by an error in the $R_{1,obs}$ estimate. Sled and Pike [142] first reported that using LL at 1.5T, a 10% error in B_1 would result in a 20% error in the estimate for F . Levesque et al. [153] also reported very high coefficient of variations for most qMT parameters in the absence of B_1 and B_0 maps, but they also used the LL methods which is much less B_1 -sensitive than VFA. Underhill et al. [165] briefly mentioned that B_1 mapping is particularly important for their whole-brain qMT implementation at 3.0T, in particular because they chose to use VFA T_1 mapping, noting that it also depends on B_1 . To the best of our knowledge, a comprehensive study aimed at characterizing the B_1 -sensitivity of qMT under these different circumstances has not been reported, which raises the following three questions: (1) what are some potential sources of B_1 -inaccuracies and how sensitive is VFA to them?, (2) are B_1 -dependent or B_1 -independent T_1 mapping methods better for

robust qMT pool-size ratio estimate?, and (3) can qMT acquisition protocols be optimized for reduced sensitivity to B_1 -inaccuracies. These questions are the focus of the manuscripts that are explored in the following three chapters, and of this PhD thesis as a whole.

Draft

1. Browne P, Chandraratna D, Angood C, Tremlett H, Baker C, Taylor BV, Thompson AJ. Atlas of Multiple Sclerosis 2013: A growing global problem with widespread inequity. *Neurology* 2014;83(11):1022-1024.
2. StatisticsCanada. Table 105-1300 - Neurological conditions, by age group and sex, household population aged 0 and over, 2010/2011, occasional (number unless otherwise noted). CANSIM (database) (accessed: 2017/11/01)
3. Orton SM, Herrera BM, Yee IM, Valdar W, Ramagopalan SV, Sadovnick AD, Ebers GC, Canadian Collaborative Study G. Sex ratio of multiple sclerosis in Canada: a longitudinal study. *Lancet Neurol* 2006;5(11):932-936.
4. Belbasis L, Bellou V, Evangelou E, Ioannidis JP, Tzoulaki I. Environmental risk factors and multiple sclerosis: an umbrella review of systematic reviews and meta-analyses. *Lancet Neurol* 2015;14(3):263-273.
5. Leray E, Moreau T, Fromont A, Edan G. Epidemiology of multiple sclerosis. *Rev Neurol (Paris)* 2016;172(1):3-13.
6. Ebers GC. Environmental factors and multiple sclerosis. *Lancet Neurol* 2008;7(3):268-277.
7. Acheson ED, Bachrach CA, Wright FM. Some Comments on the Relationship of the Distribution of Multiple Sclerosis to Latitude, Solar Radiation, and Other Variables. *Acta Psychiatrica Scandinavica* 1960;35(S147):132-147.
8. Willer CJ, Dymment DA, Sadovnick AD, Rothwell PM, Murray TJ, Ebers GC, Canadian Collaborative Study G. Timing of birth and risk of multiple sclerosis: population based study. *BMJ* 2005;330(7483):120.
9. Simpson S, Jr., Blizzard L, Otahal P, Van der Mei I, Taylor B. Latitude is significantly associated with the prevalence of multiple sclerosis: a meta-analysis. *Journal of Neurology, Neurosurgery & Psychiatry* 2011;82(10):1132-1141.
10. Willer CJ, Dymment DA, Risch NJ, Sadovnick AD, Ebers GC, Canadian Collaborative Study G. Twin concordance and sibling recurrence rates in multiple sclerosis. *Proc Natl Acad Sci U S A* 2003;100(22):12877-12882.
11. Cossburn M, Ingram G, Hirst C, Ben-Shlomo Y, Pickersgill T, Robertson N. Age at onset as a determinant of presenting phenotype and initial relapse recovery in multiple sclerosis. *Multiple Sclerosis Journal* 2012;18(1):45-54.
12. DeLuca GC, Yates RL, Beale H, Morrow SA. Cognitive Impairment in Multiple Sclerosis: Clinical, Radiologic and Pathologic Insights. *Brain Pathology* 2015;25(1):79-98.
13. Galea I, Ward-Abel N, Heesen C. Relapse in multiple sclerosis. *BMJ : British Medical Journal* 2015;350.
14. Naldi P, Collimedaglia L, Vecchio D, Rosso MG, Perl F, Stecco A, Monaco F, Leone MA. Predictors of attack severity and duration in multiple sclerosis: a prospective study. *Open Neurol J* 2011;5:75-82.
15. Saguil A, Kane S, Farnell E. Multiple sclerosis: a primary care perspective. *Am Fam Physician* 2014;90(9):644-652.
16. Atkins HL, Bowman M, Allan D, Anstee G, Arnold DL, Bar-Or A, Bence-Bruckler I, Birch P, Bredeson C, Chen J, Fergusson D, Halpenny M, Hamelin L, Huebsch L, Hutton B, Laneuville P, Lapierre Y, Lee H, Martin L, McDiarmid S, O'Connor P, Ramsay T, Sabloff M, Walker L, Freedman MS. Immunoablation and autologous

- haemopoietic stem-cell transplantation for aggressive multiple sclerosis: a multicentre single-group phase 2 trial. *Lancet* 2016;388(10044):576-585.
17. Deshmukh VA, Tardif V, Lyssiotis CA, Green CC, Kerman B, Kim HJ, Padmanabhan K, Swoboda JG, Ahmad I, Kondo T, Gage FH, Theofilopoulos AN, Lawson BR, Schultz PG, Lairson LL. A regenerative approach to the treatment of multiple sclerosis. *Nature* 2013;502(7471):327-332.
 18. Harlow DE, Honce JM, Miravalle AA. Remyelination Therapy in Multiple Sclerosis. *Front Neurol* 2015;6:257.
 19. Brown RA, Narayanan S, Arnold DL. Imaging of repeated episodes of demyelination and remyelination in multiple sclerosis. *Neuroimage Clin* 2014;6:20-25.
 20. McFarland HF, Martin R. Multiple sclerosis: a complicated picture of autoimmunity. *Nat Immunol* 2007;8(9):913-919.
 21. Perry VH. 17 - Inflammation and Axon Degeneration. In: Waxman SG, editor. *Multiple Sclerosis As A Neuronal Disease*. Burlington: Academic Press; 2005. p 241-253.
 22. Lucchinetti C, Brück W, Parisi J, Scheithauer B, Rodriguez M, Lassmann H. A quantitative analysis of oligodendrocytes in multiple sclerosis lesionsA study of 113 cases. *Brain* 1999;122(12):2279-2295.
 23. Geurts JJ, Barkhof F. Grey matter pathology in multiple sclerosis. *Lancet Neurol* 2008;7(9):841-851.
 24. Peterson JW, Bo L, Mork S, Chang A, Trapp BD. Transected neurites, apoptotic neurons, and reduced inflammation in cortical multiple sclerosis lesions. *Annals of Neurology* 2001;50(3):389-400.
 25. McDonald WI, Compston A, Edan G, Goodkin D, Hartung HP, Lublin FD, McFarland HF, Paty DW, Polman CH, Reingold SC, Sandberg-Wollheim M, Sibley W, Thompson A, van den Noort S, Weinshenker BY, Wolinsky JS. Recommended diagnostic criteria for multiple sclerosis: guidelines from the International Panel on the diagnosis of multiple sclerosis. *Ann Neurol* 2001;50(1):121-127.
 26. Polman CH, Reingold SC, Edan G, Filippi M, Hartung HP, Kappos L, Lublin FD, Metz LM, McFarland HF, O'Connor PW, Sandberg-Wollheim M, Thompson AJ, Weinshenker BG, Wolinsky JS. Diagnostic criteria for multiple sclerosis: 2005 revisions to the "McDonald Criteria". *Ann Neurol* 2005;58(6):840-846.
 27. Polman CH, Reingold SC, Banwell B, Clanet M, Cohen JA, Filippi M, Fujihara K, Havrdova E, Hutchinson M, Kappos L, Lublin FD, Montalban X, O'Connor P, Sandberg-Wollheim M, Thompson AJ, Waubant E, Weinshenker B, Wolinsky JS. Diagnostic criteria for multiple sclerosis: 2010 revisions to the McDonald criteria. *Annals of Neurology* 2011;69(2):292-302.
 28. Filippi M, Rocca MA, Ciccarelli O, De Stefano N, Evangelou N, Kappos L, Rovira A, Sastre-Garriga J, Tintore M, Frederiksen JL, Gasperini C, Palace J, Reich DS, Banwell B, Montalban X, Barkhof F, Group MS. MRI criteria for the diagnosis of multiple sclerosis: MAGNIMS consensus guidelines. *Lancet Neurol* 2016;15(3):292-303.

29. Vellinga MM, Geurts JJ, Rostrup E, Uitdehaag BM, Polman CH, Barkhof F, Vrenken H. Clinical correlations of brain lesion distribution in multiple sclerosis. *J Magn Reson Imaging* 2009;29(4):768-773.
30. Miller DH, Filippi M, Fazekas F, Frederiksen JL, Matthews PM, Montalban X, Polman CH. Role of magnetic resonance imaging within diagnostic criteria for multiple sclerosis. *Ann Neurol* 2004;56(2):273-278.
31. Anderson VM, Fox NC, Miller DH. Magnetic resonance imaging measures of brain atrophy in multiple sclerosis. *Journal of Magnetic Resonance Imaging* 2006;23(5):605-618.
32. Dalton CM, Brex PA, Jenkins R, Fox NC, Miszkiet KA, Crum WR, O'Riordan JI, Plant GT, Thompson AJ, Miller DH. Progressive ventricular enlargement in patients with clinically isolated syndromes is associated with the early development of multiple sclerosis. *Journal of Neurology, Neurosurgery & Psychiatry* 2002;73(2):141-147.
33. De Stefano N, Battaglini M, Smith SM. Measuring Brain Atrophy in Multiple Sclerosis. *Journal of Neuroimaging* 2007;17:10S-15S.
34. Horsfield MA, Rovaris M, Rocca MA, Rossi P, Benedict RHB, Filippi M, Bakshi R. Whole-brain atrophy in multiple sclerosis measured by two segmentation processes from various MRI sequences. *Journal of the Neurological Sciences* 2003;216(1):169-177.
35. Laule C, Vavasour IM, Whittall KP, Oger J, Paty DW, Li DK, MacKay AL, Arnold DL. Evolution of focal and diffuse magnetisation transfer abnormalities in multiple sclerosis. *J Neurol* 2003;250(8):924-931.
36. Rovaris M, Gass A, Bammer R, Hickman SJ, Ciccarelli O, Miller DH, Filippi M. Diffusion MRI in multiple sclerosis. *Neurology* 2005;65(10):1526-1532.
37. Schmierer K, Wheeler-Kingshott CAM, Boulby PA, Scaravilli F, Altmann DR, Barker GJ, Tofts PS, Miller DH. Diffusion tensor imaging of post mortem multiple sclerosis brain. *NeuroImage* 2007;35(2):467-477.
38. Schmierer K, Scaravilli F, Altmann DR, Barker GJ, Miller DH. Magnetization transfer ratio and myelin in postmortem multiple sclerosis brain. *Annals of Neurology* 2004;56(3):407-415.
39. Schmierer K, Tozer DJ, Scaravilli F, Altmann DR, Barker GJ, Tofts PS, Miller DH. Quantitative magnetization transfer imaging in postmortem multiple sclerosis brain. *J Magn Reson Imaging* 2007;26(1):41-51.
40. Loitfelder M, Fazekas F, Petrovic K, Fuchs S, Ropele S, Wallner-Blazek M, Jehna M, Aspeck E, Khalil M, Schmidt R, Neuper C, Enzinger C. Reorganization in cognitive networks with progression of multiple sclerosis: Insights from fMRI. *Neurology* 2011;76(6):526-533.
41. Rocca MA, Colombo B, Falini A, Ghezzi A, Martinelli V, Scotti G, Comi G, Filippi M. Cortical adaptation in patients with MS: a cross-sectional functional MRI study of disease phenotypes. *The Lancet Neurology* 2005;4(10):618-626.
42. Schmierer K, Thavarajah JR, An SF, Brandner S, Miller DH, Tozer DJ. Effects of formalin fixation on magnetic resonance indices in multiple sclerosis cortical gray matter. *J Magn Reson Imaging* 2010;32(5):1054-1060.

43. Chen JTH, Easley K, Schneider C, Nakamura K, Kidd GJ, Chang A, Staugaitis SM, Fox RJ, Fisher E, Arnold DL, Trapp BD. Clinically feasible MTR is sensitive to cortical demyelination in MS. *Neurology* 2013;80(3):246-252.
44. Derakhshan M, Caramanos Z, Giacomini PS, Narayanan S, Maranzano J, Francis SJ, Arnold DL, Collins DL. Evaluation of automated techniques for the quantification of grey matter atrophy in patients with multiple sclerosis. *NeuroImage* 2010;52(4):1261-1267.
45. Derakhshan M, Caramanos Z, Narayanan S, Arnold DL, Louis Collins D. Surface-based analysis reveals regions of reduced cortical magnetization transfer ratio in patients with multiple sclerosis: A proposed method for imaging subpial demyelination. *Human Brain Mapping* 2014;35(7):3402-3413.
46. Rudko DA, Derakhshan M, Maranzano J, Nakamura K, Arnold DL, Narayanan S. Delineation of cortical pathology in multiple sclerosis using multi-surface magnetization transfer ratio imaging. *Neuroimage Clin* 2016;12:858-868.
47. Narayanan A, Hartman JS, Bain AD. Characterizing Nonexponential Spin-Lattice Relaxation in Solid-State NMR by Fitting to the Stretched Exponential. *Journal of Magnetic Resonance, Series A* 1995;112(1):58-65.
48. Di Giovanni P, Azlan CA, Ahearn TS, Semple SI, Gilbert FJ, Redpath TW. The accuracy of pharmacokinetic parameter measurement in DCE-MRI of the breast at 3 T. *Physics in Medicine & Biology* 2010;55(1):121-132.
49. Yuan J, Chow SK, Yeung DK, Ahuja AT, King AD. Quantitative evaluation of dual-flip-angle T1 mapping on DCE-MRI kinetic parameter estimation in head and neck. *Quant Imaging Med Surg* 2012;2(4):245-253.
50. Drain LE. A Direct Method of Measuring Nuclear Spin-Lattice Relaxation Times. *Proceedings of the Physical Society of London Section A* 1949;62(353):301-306.
51. Hahn EL. An Accurate Nuclear Magnetic Resonance Method for Measuring Spin-Lattice Relaxation Times. *Physical Review* 1949;76(1):145-146.
52. Barral JK, Gudmundson E, Stikov N, Etezadi-Amoli M, Stoica P, Nishimura DG. A robust methodology for in vivo T1 mapping. *Magn Reson Med* 2010;64(4):1057-1067.
53. Stikov N, Boudreau M, Levesque IR, Tardif CL, Barral JK, Pike GB. On the accuracy of T1 mapping: searching for common ground. *Magn Reson Med* 2015;73(2):514-522.
54. Look DC, Locker DR. Time Saving in Measurement of NMR and EPR Relaxation Times. *Review of Scientific Instruments* 1970;41(2):250-251.
55. Crawley AP, Henkelman RM. A comparison of one-shot and recovery methods in T1 imaging. *Magn Reson Med* 1988;7(1):23-34.
56. Marques JP, Kober T, Krueger G, van der Zwaag W, Van de Moortele PF, Gruetter R. MP2RAGE, a self bias-field corrected sequence for improved segmentation and T1-mapping at high field. *Neuroimage* 2010;49(2):1271-1281.
57. Kober T, Granziere C, Ribes D, Browaeys P, Schluep M, Meuli R, Frackowiak R, Gruetter R, Krueger G. MP2RAGE Multiple Sclerosis Magnetic Resonance Imaging at 3 T. *Investigative Radiology* 2012;47(6):346-352.
58. Fram EK, Herfkens RJ, Johnson GA, Glover GH, Karis JP, Shimakawa A, Perkins TG, Pelc NJ. Rapid Calculation of T1 Using Variable Flip Angle Gradient Refocused Imaging. *Magnetic Resonance Imaging* 1987;5(3):201-208.

59. Cheng HL, Wright GA. Rapid high-resolution T(1) mapping by variable flip angles: accurate and precise measurements in the presence of radiofrequency field inhomogeneity. *Magn Reson Med* 2006;55(3):566-574.
60. Deoni SC, Rutt BK, Peters TM. Rapid combined T1 and T2 mapping using gradient recalled acquisition in the steady state. *Magn Reson Med* 2003;49(3):515-526.
61. Liberman G, Louzoun Y, Ben Bashat D. T(1) mapping using variable flip angle SPGR data with flip angle correction. *J Magn Reson Imaging* 2014;40(1):171-180.
62. Leppert IR, Narayanan S, Araujo D, Giacomini PS, Lapierre Y, Arnold DL, Pike GB. Interpreting therapeutic effect in multiple sclerosis via MRI contrast enhancing lesions: now you see them, now you don't. *J Neurol* 2014;261(4):809-816.
63. Sung K, Daniel BL, Hargreaves BA. Transmit B1+ field inhomogeneity and T1 estimation errors in breast DCE-MRI at 3 tesla. *J Magn Reson Imaging* 2013;38(2):454-459.
64. Traficante DD. Relaxation. Can T2, be longer than T1? Concepts in Magnetic Resonance 1991;3(3):171-177.
65. Anet FAL, O'Leary DJ. The shielding tensor part II: Understanding its strange effects on relaxation. Concepts in Magnetic Resonance 1992;4(1):35-52.
66. Budimir J, Skinner JL. On the relationship between T1 and T2 for stochastic relaxation models. *Journal of Statistical Physics* 1987;49(5):1029-1042.
67. Sevan HM, Skinner JL. T2 can be greater than 2T1. *The Journal of Chemical Physics* 1989;91(3):1775-1782.
68. Bojorquez JZ, Bricq S, Acqutter C, Brunotte F, Walker PM, Lalande A. What are normal relaxation times of tissues at 3 T? *Magnetic Resonance Imaging* 2017;35(Supplement C):69-80.
69. Fullerton GD, Potter JL, Dornbluth NC. NMR relaxation of protons in tissues and other macromolecular water solutions. *Magnetic Resonance Imaging* 1982;1(4):209-226.
70. Bloembergen N, Purcell EM, Pound RV. Relaxation Effects in Nuclear Magnetic Resonance Absorption. *Physical Review* 1948;73(7):679-712.
71. Li TQ, Yao B, van Gelderen P, Merkle H, Dodd S, Talagala L, Koretsky AP, Duyn J. Characterization of T(2)* heterogeneity in human brain white matter. *Magn Reson Med* 2009;62(6):1652-1657.
72. Underhill HR, Rostomily RC, Mikheev AM, Yuan C, Yarnykh VL. Fast bound pool fraction imaging of the in vivo rat brain: association with myelin content and validation in the C6 glioma model. *NeuroImage* 2011;54(3):2052-2065.
73. Mackay A, Whittall K, Adler J, Li D, Paty D, Graeb D. In vivo visualization of myelin water in brain by magnetic resonance. *Magnetic Resonance in Medicine* 1994;31(6):673-677.
74. MacKay A, Laule C, Vavasour I, Bjarnason T, Kolind S, Madler B. Insights into brain microstructure from the T2 distribution. *Magn Reson Imaging* 2006;24(4):515-525.
75. Moore GR, Leung E, MacKay AL, Vavasour IM, Whittall KP, Cover KS, Li DK, Hashimoto SA, Oger J, Sprinkle TJ, Paty DW. A pathology-MRI study of the short-T2 component in formalin-fixed multiple sclerosis brain. *Neurology* 2000;55(10):1506-1510.

76. Laule C, Yung A, Pavolva V, Bohnet B, Kozlowski P, Hashimoto SA, Yip S, Li DK, Moore GW. High-resolution myelin water imaging in post-mortem multiple sclerosis spinal cord: A case report. *Mult Scler* 2016;22(11):1485-1489.
77. Alonso-Ortiz E, Levesque IR, Pike GB. MRI-based myelin water imaging: A technical review. *Magnetic Resonance in Medicine* 2015;73(1):70-81.
78. Collins CM, Wang Z. Calculation of radiofrequency electromagnetic fields and their effects in MRI of human subjects. *Magnetic Resonance in Medicine* 2011;65(5):1470-1482.
79. Liu J, Zhang X, Schmitter S, Van de Moortele PF, He B. Gradient-based electrical properties tomography (gEPT): A robust method for mapping electrical properties of biological tissues in vivo using magnetic resonance imaging. *Magn Reson Med* 2015;74(3):634-646.
80. Katscher U, Voigt T, Findekle C, Vernickel P, Nehrke K, Dossel O. Determination of electric conductivity and local SAR via B1 mapping. *IEEE Trans Med Imaging* 2009;28(9):1365-1374.
81. Jin J, Chen J. On the SAR and field inhomogeneity of birdcage coils loaded with the human head. *Magn Reson Med* 1997;38(6):953-963.
82. Sled JG, Pike GB. Standing-wave and RF penetration artifacts caused by elliptic geometry: an electrodynamic analysis of MRI. *IEEE Trans Med Imaging* 1998;17(4):653-662.
83. Van de Moortele P-F, Akgun C, Adriany G, Moeller S, Ritter J, Collins CM, Smith MB, Vaughan JT, Uğurbil K. B1 destructive interferences and spatial phase patterns at 7 T with a head transceiver array coil. *Magnetic Resonance in Medicine* 2005;54(6):1503-1518.
84. Insko EK, Bolinger L. Mapping of the Radiofrequency Field. *Journal of Magnetic Resonance Series A* 1993;103(1):82-85.
85. Stollberger R, Wach P. Imaging of the active B1 field in vivo. *Magnetic Resonance in Medicine* 1996;35(2):246-251.
86. Wang J, Qiu M, Constable RT. In vivo method for correcting transmit/receive nonuniformities with phased array coils. *Magn Reson Med* 2005;53(3):666-674.
87. Samson RS, Wheeler-Kingshott CA, Symms MR, Tozer DJ, Tofts PS. A simple correction for B1 field errors in magnetization transfer ratio measurements. *Magn Reson Imaging* 2006;24(3):255-263.
88. Sled JG, Pike GB. Correction for B1 and B0 variations in quantitative T2 measurements using MRI. *Magnetic Resonance in Medicine* 2000;43(4):589-593.
89. Yarnykh VL. Actual flip-angle imaging in the pulsed steady state: a method for rapid three-dimensional mapping of the transmitted radiofrequency field. *Magn Reson Med* 2007;57(1):192-200.
90. Sacolick LI, Wiesinger F, Hancu I, Vogel MW. B1 mapping by Bloch-Siegert shift. *Magn Reson Med* 2010;63(5):1315-1322.
91. Nehrke K. On the steady-state properties of actual flip angle imaging (AFI). *Magn Reson Med* 2009;61(1):84-92.
92. Yarnykh VL. Optimal radiofrequency and gradient spoiling for improved accuracy of T1 and B1 measurements using fast steady-state techniques. *Magn Reson Med* 2010;63(6):1610-1626.

93. Pohmann R, Scheffler K. A theoretical and experimental comparison of different techniques for B(1) mapping at very high fields. *NMR Biomed* 2013;26(3):265-275.
94. Versluis MJ, Tsekos N, Smith NB, Webb AG. Simple RF design for human functional and morphological cardiac imaging at 7tesla. *Journal of Magnetic Resonance* 2009;200(1):161-166.
95. Zhang B, Seifert AC, Kim J-w, Borrello J, Xu J. 7 Tesla 22-channel wrap-around coil array for cervical spinal cord and brainstem imaging. *Magnetic Resonance in Medicine* 2017;78(4):1623-1634.
96. Avdievich NI, Giapitzakis IA, Pfrommer A, Henning A. Decoupling of a tight-fit transceiver phased array for human brain imaging at 9.4T: Loop overlapping rediscovered. *Magn Reson Med* 2017;n/a-n/a.
97. Chavez S, Xiang QS, An L. Understanding phase maps in MRI: a new cutline phase unwrapping method. *IEEE Trans Med Imaging* 2002;21(8):966-977.
98. Clarke WT, Robson MD, Rodgers CT. Bloch-Siebert B1+-mapping for human cardiac 31P-MRS at 7 Tesla. *Magnetic Resonance in Medicine* 2016;76(4):1047-1058.
99. Schneider E, Glover G. Rapid in vivo proton shimming. *Magnetic Resonance in Medicine* 1991;18(2):335-347.
100. Edzes HT, Samulski ET. Cross relaxation and spin diffusion in the proton NMR of hydrated collagen. *Nature* 1977;265(5594):521-523.
101. Edzes HT, Samulski ET. The measurement of cross-relaxation effects in the proton NMR spin-lattice relaxation of water in biological systems: Hydrated collagen and muscle. *Journal of Magnetic Resonance* (1969) 1978;31(2):207-229.
102. Wolff SD, Balaban RS. Magnetization transfer contrast (MTC) and tissue water proton relaxation in vivo. *Magn Reson Med* 1989;10(1):135-144.
103. Levesque IR, Pike GB. Characterizing healthy and diseased white matter using quantitative magnetization transfer and multicomponent T(2) relaxometry: A unified view via a four-pool model. *Magn Reson Med* 2009;62(6):1487-1496.
104. Dixon WT, Engels H, Castillo M, Sardashti M. Incidental magnetization transfer contrast in standard multislice imaging. *Magn Reson Imaging* 1990;8(4):417-422.
105. Santyr GE. Magnetization transfer effects in multislice MR imaging. *Magn Reson Imaging* 1993;11(4):521-532.
106. Berry I, Barker GJ, Barkhof F, Campi A, Dousset V, Franconi J-M, Gass A, Schreiber W, Miller DH, Tofts PS. A multicenter measurement of magnetization transfer ratio in normal white matter. *Journal of Magnetic Resonance Imaging* 1999;9(3):441-446.
107. Horsfield MA, Barker GJ, Barkhof F, Miller DH, Thompson AJ, Filippi M. Guidelines for using quantitative magnetization transfer magnetic resonance imaging for monitoring treatment of multiple sclerosis. *Journal of Magnetic Resonance Imaging* 2003;17(4):389-397.
108. Barker GJ, Schreiber WG, Gass A, Ranjeva JP, Campi A, Waesberghe JHTMv, Franconi J-M, Watt HC, Tofts PS. A standardised method for measuring magnetisation transfer ratio on MR imagers from different manufacturers—the EuroMT sequence. *Magnetic Resonance Materials in Physics, Biology and Medicine* 2005;18(2):76-80.

109. Ropele S, Filippi M, Valsasina P, Korteweg T, Barkhof F, Tofts PS, Samson R, Miller DH, Fazekas F. Assessment and correction of B1-induced errors in magnetization transfer ratio measurements. *Magn Reson Med* 2005;53(1):134-140.
110. Levesque I, Sled JG, Narayanan S, Santos AC, Brass SD, Francis SJ, Arnold DL, Pike GB. The role of edema and demyelination in chronic T1 black holes: a quantitative magnetization transfer study. *J Magn Reson Imaging* 2005;21(2):103-110.
111. Van Waesberghe JHTM, Kamphorst W, De Groot CJA, Van Walderveen MAA, Castelijns JA, Ravid R, Lycklama à Nijeholt GJ, Van Der Valk P, Polman CH, Thompson AJ, Barkhof F. Axonal loss in multiple sclerosis lesions: Magnetic resonance imaging insights into substrates of disability. *Annals of Neurology* 1999;46(5):747-754.
112. Dousset V, Gayou A, Brochet B, Caille J-M. Early structural changes in acute MS lesions assessed by serial magnetization transfer studies. *Neurology* 1998;51(4):1150-1155.
113. Chen JT, Collins DL, Atkins HL, Freedman MS, Arnold DL. Magnetization transfer ratio evolution with demyelination and remyelination in multiple sclerosis lesions. *Annals of Neurology* 2008;63(2):254-262.
114. Altmann DR, Button T, Schmierer K, Hunter K, Tozer DJ, Wheeler-Kingshott CA, Coles A, Miller DH. Sample sizes for lesion magnetisation transfer ratio outcomes in remyelination trials for multiple sclerosis. *Multiple Sclerosis and Related Disorders* 2014;3(2):237-243.
115. Traboulsee A, Dehmeshki J, Peters KR, Griffin CM, Brex PA, Silver N, Ciccarrelli O, Chard DT, Barker GJ, Thompson AJ, Miller DH. Disability in multiple sclerosis is related to normal appearing brain tissue MTR histogram abnormalities. *Multiple Sclerosis Journal* 2003;9(6):566-573.
116. Mangia S, Carpenter AF, Tyan AE, Eberly LE, Garwood M, Michaeli S. Magnetization transfer and adiabatic T1rho MRI reveal abnormalities in normal-appearing white matter of subjects with multiple sclerosis. *Mult Scler* 2014;20(8):1066-1073.
117. Vrenken H, Pouwels PJ, Ropele S, Knol DL, Geurts JJ, Polman CH, Barkhof F, Castelijns JA. Magnetization transfer ratio measurement in multiple sclerosis normal-appearing brain tissue: limited differences with controls but relationships with clinical and MR measures of disease. *Mult Scler* 2007;13(6):708-716.
118. Fisniku LK, Altmann DR, Cercignani M, Tozer DJ, Chard DT, Jackson JS, Miszkiel KA, Schmierer K, Thompson AJ, Miller DH. Magnetization transfer ratio abnormalities reflect clinically relevant grey matter damage in multiple sclerosis. *Mult Scler* 2009;15(6):668-677.
119. Chen JT, Collins DL, Freedman MS, Atkins HL, Arnold DL, Canadian MSBMTSG. Local magnetization transfer ratio signal inhomogeneity is related to subsequent change in MTR in lesions and normal-appearing white-matter of multiple sclerosis patients. *Neuroimage* 2005;25(4):1272-1278.
120. Crespy L, Zaaraoui W, Lemaire M, Rico A, Faivre A, Reuter F, Malikova I, Confort-Gouny S, Cozzzone PJ, Pelletier J, Ranjeva JP, Audoin B. Prevalence of grey matter pathology in early multiple sclerosis assessed by magnetization transfer ratio imaging. *PLoS One* 2011;6(9):e24969.

121. Audoin B, Ranjeva J-P, Duong MVA, Ibarrola D, Malikova I, Confort-Gouny S, Soulier E, Viout P, Ali-Chérif A, Pelletier J, Cozzzone PJ. Voxel-based analysis of MTR images: A method to locate gray matter abnormalities in patients at the earliest stage of multiple sclerosis. *Journal of Magnetic Resonance Imaging* 2004;20(5):765-771.
122. Richert ND, Ostuni JL, Bash CN, Leist TP, McFarland HF, Frank JA. Interferon beta-1b and intravenous methylprednisolone promote lesion recovery in multiple sclerosis. *Multiple Sclerosis Journal* 2001;7(1):49-58.
123. Kita M, Goodkin DE, Bacchetti P, Waubant E, Nelson SJ, Majumdar S. Magnetization transfer ratio in new MS lesions before and during therapy with IFN β -1a. *Neurology* 2000;54(9):1741-1745.
124. Button T, Altmann D, Tozer D, Dalton C, Hunter K, Compston A, Coles A, Miller D. Magnetization transfer imaging in multiple sclerosis treated with alemtuzumab. *Mult Scler* 2013;19(2):241-244.
125. Tao Y, Zhang X, Zivadinov R, Dwyer MG, Kennedy C, Bergsland N, Ramasamy D, Durfee J, Hojnacki D, Hayward B, Dangond F, Weinstock-Guttman B, Markovic-Plese S. Immunologic and MRI markers of the therapeutic effect of IFN-beta-1a in relapsing-remitting MS. *Neurol Neuroimmunol Neuroinflamm* 2015;2(6):e176.
126. Kubicki M, Park H, Westin CF, Nestor PG, Mulkern RV, Maier SE, Niznikiewicz M, Connor EE, Levitt JJ, Frumin M, Kikinis R, Jolesz FA, McCarley RW, Shenton ME. DTI and MTR abnormalities in schizophrenia: analysis of white matter integrity. *Neuroimage* 2005;26(4):1109-1118.
127. Antosik-Biernacka A, Peuskens H, De Hert M, Peuskens J, Sunaert S, Van Hecke P, Goraj B. Magnetization transfer imaging in chronic schizophrenia. *Med Sci Monit* 2006;12(4):MT17-21.
128. Ge Y, Kolson DL, Babb JS, Mannon LJ, Grossman RI. Whole brain imaging of HIV-infected patients: quantitative analysis of magnetization transfer ratio histogram and fractional brain volume. *AJNR Am J Neuroradiol* 2003;24(1):82-87.
129. Fornari E, Maeder P, Meuli R, Ghika J, Knyazeva MG. Demyelination of superficial white matter in early Alzheimer's disease: a magnetization transfer imaging study. *Neurobiol Aging* 2012;33(2):428 e427-419.
130. Chen Z, Zhang H, Jia Z, Zhong J, Huang X, Du M, Chen L, Kuang W, Sweeney JA, Gong Q. Magnetization transfer imaging of suicidal patients with major depressive disorder. *Sci Rep* 2015;5:9670.
131. Helms G, Dathe H, Kallenberg K, Dechent P. High-resolution maps of magnetization transfer with inherent correction for RF inhomogeneity and T1 relaxation obtained from 3D FLASH MRI. *Magnetic Resonance in Medicine* 2008;60(6):1396-1407.
132. Helms G, Dathe H, Kallenberg K, Dechent P. High-resolution maps of magnetization transfer with inherent correction for Rf inhomogeneity and T-1 relaxation obtained from 3D FLASH MRI (vol 60, pg 1396, 2008). *Magnetic Resonance in Medicine* 2010;64(6):1856-1856.
133. Lema A, Bishop C, Malik O, Mattoscio M, Ali R, Nicholas R, Muraro PA, Matthews PM, Waldman AD, Newbould RD. A Comparison of Magnetization

- Transfer Methods to Assess Brain and Cervical Cord Microstructure in Multiple Sclerosis. *Journal of Neuroimaging* 2017;27(2):221-226.
134. Campbell JSW, Leppert IR, Narayanan S, Boudreau M, Duval T, Cohen-Adad J, Pike GB, Stikov N. Promise and pitfalls of g-ratio estimation with MRI. *NeuroImage* 2017.
 135. Mohammadi S, Carey D, Dick F, Diedrichsen J, Sereno MI, Reisert M, Callaghan MF, Weiskopf N. Whole-Brain In-vivo Measurements of the Axonal G-Ratio in a Group of 37 Healthy Volunteers. *Frontiers in Neuroscience* 2015;9(441).
 136. Helms G, Draganski B, Frackowiak R, Ashburner J, Weiskopf N. Improved segmentation of deep brain grey matter structures using magnetization transfer (MT) parameter maps. *NeuroImage* 2009;47(1):194-198.
 137. Helms G. Volume correction for edema in single-volume proton MR spectroscopy of contrast-enhancing multiple sclerosis lesions. *Magn Reson Med* 2001;46(2):256-263.
 138. Solomon I. Relaxation Processes in a System of Two Spins. *Physical Review* 1955;99(2):559-565.
 139. Bloembergen N, Shapiro S, Pershan PS, Artman JO. Cross-Relaxation in Spin Systems. *Physical Review* 1959;114(2):445-459.
 140. Henkelman RM, Huang X, Xiang QS, Stanisz GJ, Swanson SD, Bronskill MJ. Quantitative interpretation of magnetization transfer. *Magn Reson Med* 1993;29(6):759-766.
 141. Sled JG, Pike GB. Quantitative interpretation of magnetization transfer in spoiled gradient echo MRI sequences. *Journal of Magnetic Resonance* 2000;145(1):24-36.
 142. Sled JG, Pike GB. Quantitative imaging of magnetization transfer exchange and relaxation properties in vivo using MRI. *Magn Reson Med* 2001;46(5):923-931.
 143. Morrison C, Henkelman RM. A model for magnetization transfer in tissues. *Magn Reson Med* 1995;33(4):475-482.
 144. Hu BS, Conolly SM, Wright GA, Nishimura DG, Macovski A. Pulsed saturation transfer contrast. *Magnetic Resonance in Medicine* 1992;26(2):231-240.
 145. Pike GB, Glover GH, Hu BS, Enzmann DR. Pulsed magnetization transfer spin-echo MR imaging. *Journal of Magnetic Resonance Imaging* 1993;3(3):531-539.
 146. Listerud J. Off-resonance pulsed magnetization transfer in clinical MR imaging: Optimization by an analysis of transients. *Magnetic Resonance in Medicine* 1997;37(5):693-705.
 147. Ramani A, Dalton C, Miller DH, Tofts PS, Barker GJ. Precise estimate of fundamental in-vivo MT parameters in human brain in clinically feasible times. *Magn Reson Imaging* 2002;20(10):721-731.
 148. Yarnykh VL. Pulsed Z-spectroscopic imaging of cross-relaxation parameters in tissues for human MRI: theory and clinical applications. *Magn Reson Med* 2002;47(5):929-939.
 149. Portnoy S, Stanisz GJ. Modeling pulsed magnetization transfer. *Magn Reson Med* 2007;58(1):144-155.
 150. Cabana J-F, Gu Y, Boudreau M, Levesque IR, Atchia Y, Sled JG, Narayanan S, Arnold DL, Pike GB, Cohen-Adad J, Duval T, Vuong M-T, Stikov N. Quantitative magnetization transfer imaging made easy with qMTLab: Software for data

- simulation, analysis, and visualization. *Concepts in Magnetic Resonance Part A* 2015;44A(5):263-277.
151. Levesque IR, Giacomini PS, Narayanan S, Ribeiro LT, Sled JG, Arnold DL, Pike GB. Quantitative magnetization transfer and myelin water imaging of the evolution of acute multiple sclerosis lesions. *Magn Reson Med* 2010;63(3):633-640.
 152. Sled JG, Levesque I, Santos AC, Francis SJ, Narayanan S, Brass SD, Arnold DL, Pike GB. Regional variations in normal brain shown by quantitative magnetization transfer imaging. *Magnetic Resonance in Medicine* 2004;51(2):299-303.
 153. Levesque IR, Sled JG, Narayanan S, Giacomini PS, Ribeiro LT, Arnold DL, Pike GB. Reproducibility of quantitative magnetization-transfer imaging parameters from repeated measurements. *Magn Reson Med* 2010;64(2):391-400.
 154. Rausch M, Tofts P, Lervik P, Walmsley A, Mir A, Schubart A, Seabrook T. Characterization of white matter damage in animal models of multiple sclerosis by magnetization transfer ratio and quantitative mapping of the apparent bound proton fraction f . *Mult Scler* 2009;15(1):16-27.
 155. Turati L, Moscatelli M, Mastropietro A, Dowell NG, Zucca I, Erbetta A, Cordiglieri C, Brenna G, Bianchi B, Mantegazza R, Cercignani M, Baggi F, Minati L. In vivo quantitative magnetization transfer imaging correlates with histology during de- and remyelination in cuprizone-treated mice. *NMR Biomed* 2015;28(3):327-337.
 156. Giulietti G, Bozzali M, Figura V, Spano B, Perri R, Marra C, Lacidogna G, Giubilei F, Caltagirone C, Cercignani M. Quantitative magnetization transfer provides information complementary to grey matter atrophy in Alzheimer's disease brains. *Neuroimage* 2012;59(2):1114-1122.
 157. Arlinghaus LR, Dortch RD, Whisenant JG, Kang H, Abramson RG, Yankeelov TE. Quantitative Magnetization Transfer Imaging of the Breast at 3.0 T: Reproducibility in Healthy Volunteers. *Tomography : a journal for imaging research* 2016;2(4):260-266.
 158. Stikov N, Keenan KE, Pauly JM, Smith RL, Dougherty RF, Gold GE. Cross-relaxation imaging of human articular cartilage. *Magn Reson Med* 2011;66(3):725-734.
 159. Stikov N, Campbell JS, Stroh T, Lavelee M, Frey S, Novek J, Nuara S, Ho MK, Bedell BJ, Dougherty RF, Leppert IR, Boudreau M, Narayanan S, Duval T, Cohen-Adad J, Picard PA, Gasecka A, Cote D, Pike GB. In vivo histology of the myelin g-ratio with magnetic resonance imaging. *Neuroimage* 2015;118:397-405.
 160. Bajd F, Škrlep M, Čandek-Potokar M, Vidmar J, Serša I. Application of quantitative magnetization transfer magnetic resonance imaging for characterization of dry-cured hams. *Meat Science* 2016;122(Supplement C):109-118.
 161. Cercignani M, Alexander DC. Optimal acquisition schemes for in vivo quantitative magnetization transfer MRI. *Magn Reson Med* 2006;56(4):803-810.
 162. Levesque IR, Sled JG, Pike GB. Iterative optimization method for design of quantitative magnetization transfer imaging experiments. *Magn Reson Med* 2011;66(3):635-643.
 163. Lustig M, Donoho D, Pauly JM. Sparse MRI: The application of compressed sensing for rapid MR imaging. *Magn Reson Med* 2007;58(6):1182-1195.

164. Lustig M, Pauly JM. SPIRiT: Iterative self-consistent parallel imaging reconstruction from arbitrary k-space. *Magn Reson Med* 2010;64(2):457-471.
165. Underhill HR, Yuan C, Yarnykh VL. Direct quantitative comparison between cross-relaxation imaging and diffusion tensor imaging of the human brain at 3.0 T. *Neuroimage* 2009;47(4):1568-1578.

Draft